

An architecture for quantum networking of neutral atom processors

C. B. Young, A. Safari, P. Huft, J. Zhang, E. Oh, R. Chinnarasu, and M. Saffman
Department of Physics, University of Wisconsin-Madison, Madison, WI, 53706

(Dated: 22 June 2022)

Development of a network for remote entanglement of quantum processors is an outstanding challenge in quantum information science. We propose and analyze a two-species architecture for remote entanglement of neutral atom quantum computers based on integration of optically trapped atomic qubit arrays with fast optics for photon collection. One of the atomic species is used for atom-photon entanglement, and the other species provides local processing. We compare the achievable rates of remote entanglement generation for two optical approaches: free space photon collection with a lens and a near-concentric, long working distance resonant cavity. Laser cooling and trapping within the cavity removes the need for mechanical transport of atoms from a source region, which allows for a fast repetition rate. Using optimized values of the cavity finesse, remote entanglement generation rates $> 10^3 \text{ s}^{-1}$ are predicted for experimentally feasible parameters.

I. INTRODUCTION

An outstanding challenge in the field of quantum information science is the ability to connect multiple quantum processors or sensors in a quantum network. This capability will enable distributed quantum computation and sensing, as well as secure long distance communication based on networked quantum repeaters, each containing an interface between stationary and flying qubits, quantum memory, and processing capability. Moreover, at any stage of the development of quantum computers, there may be a practical limitation on the achievable number of qubits in a single processing unit. Therefore, quantum networks will enable a route towards building a large scale quantum processor based on a modular architecture¹.

The backbone of such a network is quantum entanglement distributed among the nodes. In this paper we analyze a quantum network architecture based on interconnected functional nodes, each containing memory and processing, as well as an interface between matter qubits and photons that mediate entanglement distribution. A conceptual illustration of such a network based on neutral atoms is provided in Fig. 1. Each node contains a neutral atom quantum processor that provides memory and logic². The emergent capabilities of neutral atom arrays for circuit model quantum computation have recently been established^{3,4}. Multi-qubit logic is enabled by excitation to Rydberg states which provide strong entangling interactions⁵.

In order to achieve entanglement distribution at high rates it is desirable to either collect scattered light with a high numerical aperture (NA) lens, or to strongly couple atoms and photons in a resonant cavity. Practical architectures for strong coupling of atoms to photons often involve placing the atoms close to material surfaces. This is problematic when Rydberg states are used for quantum logic since these states are strongly perturbed by electric fields arising from surface charges. This renders nanophotonic devices for strong atom-photon coupling⁶⁻⁹ challenging to incorporate in node architectures that utilize Rydberg state operations.

For this reason we will consider approaches that have the potential to reach high rates of entanglement distribution without requiring atoms to be closer than a few mm from the nearest surface. We analyze two primary designs: free space collection of emitted photons with a high NA, yet long working distance, lens or mirror, and atom-photon coupling in a linear resonator. This leads to the type of architecture shown in Fig. 1 where an atomic qubit array is located inside a few mm - cm scale optical resonator. In order to achieve strong coupling without requiring a very short resonator length we concentrate on a near-concentric resonator design¹⁰⁻¹². In a free space version the resonator is replaced by a single collection lens. Note that with the $3 \mu\text{m}$ qubit spacing demonstrated recently³, even a large array with 10^5 qubits only occupies a square of size 1 mm^2 and can thus be easily located inside a cm scale resonator.

A variety of approaches are possible for mediating atom-photon entanglement in each node¹³⁻¹⁵, including the use of Rydberg states to provide directional single photon emission¹⁶⁻²⁰. The need to protect memory coherence in a multi-qubit processor while also enabling a fast qubit-photon interface is a key architectural challenge. We propose a solution based on a dual species architecture: one type of atom is used for memory and processing, and another type is used for communication and atom-photon coupling. Memory and communication qubits are coupled via interspecies Rydberg gates²¹, while the optical wavelengths used to couple to communication qubits do not perturb the memory atoms. In a two-species architecture the communication qubits can also be used for non-destructive state measurements without crosstalk to data qubits, which will enable measurement based error correction protocols²². This type of large, two-species atomic array was demonstrated recently²³. Analogous ideas have been developed for two-species trapped ion networking²⁴. Alternatively a single atomic species can be used provided that data qubits that would interact with communication light can be shelved in states that are dark with respect to transitions involved in mediating atom-photon entanglement²⁵, or coherently transferred to other states as needed for

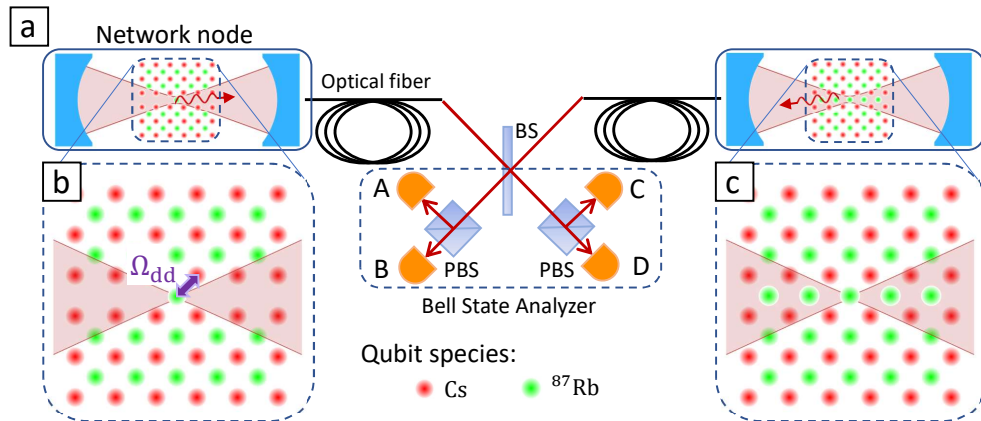


FIG. 1. a) Illustration of two neutral atom quantum registers connected by a photonic link. Two schemes are shown for mediating the transfer of atomic excitations onto photon polarization states: b) a single atom interacting with the cavity mode, and c) multiple atoms interacting with the cavity mode. Entanglement between a register atom and communication atom(s) at each node is mediated by Rydberg interactions, indicated by Ω_{dd} . Coherent scattering of photons from the single Rb atoms results in atom-photon entanglement at each node, which is projected onto atom-atom entanglement upon interference at the Bell state analyzer. The measurement requires a 50:50 beam splitter (BS), two polarizing beam splitters (PBS) and four single-photon counting modules (labeled A to D).

communication^{7,26}. While a detailed comparison of two-species and one-species architectures is premature at this time a few comments may be made. Laser cooling and control of two-species requires a significant overhead of additional laser systems and optics, but enables a very low level of crosstalk due to the difference in interaction wavelengths. A single species solution is likely to require less infrastructure, but may require more operations to isolate communication and processing functionalities, and suffer from higher crosstalk when implemented in the ground manifold of an alkali atom. Recent proposals for quantum networking with Yb atoms may provide more favorable single species solutions⁷.

In the simplest version of this architecture a single communication qubit couples to the light, This can be extended to optical coupling of several communication qubits which enables generation of complex, multi-mode optical quantum states²⁷. It is also possible to combine a sequence of memory-communication qubit entanglement and communication qubit - photon entanglement steps into a single interaction where an ensemble of communication atoms directly mediates entanglement between a single addressed memory qubit and a photon, even though the optical wavelength does not directly interact with memory qubit transitions²⁸. This approach can form the basis of a multi-node network for distributed computation²⁹.

In the rest of this paper we focus on entanglement of a single communication qubit with a photon using the protocol introduced in Ref.¹³. Coherent scattering of photons by a suitably prepared ⁸⁷Rb atom leads to entanglement between the atom and a scattered photon which is collected by the aid of a lens or optical cavity and coupled

into a single-mode fiber. A Bell state measurement of the entangled photons from two nodes results in probabilistic but heralded entanglement between the two ⁸⁷Rb atoms. Local gates between communication and data qubits at each node can then be used to entangle multi-qubit states between nodes.

The Bell state measurement with four detectors enable remote atom-atom entanglement with a success probability of at most 50%³⁰. Although the probabilistic nature of the entanglement in this protocol does not prevent the creation of a quantum network, increasing the success probability is essential to achieve an efficient network. As we discuss below, the photon collection efficiency is often the main limiting factor for the overall success probability. Therefore, it is crucial to improve the collection efficiency to achieve a scalable quantum network.

We compare photon collection approaches using high NA optics (lenses and parabolic mirrors) with optical cavities. We show that a properly designed optical cavity can improve the photon collection efficiency significantly. We consider near-concentric cavities where the large separation of the cavity mirrors allows for cooling and trapping of the atoms directly inside the cavity.

Furthermore, we analyze the case of a two-node quantum network where each node consists of a single Rb atom coupled to a near-concentric cavity. We calculate the success probability and estimate the rate of atom-atom entanglement. We show that by using a non-destructive readout of the atomic states and incorporating optical cavities, an entanglement generation rate up to a few thousand s^{-1} is in principle achievable.

The rest of the paper is organized as follows. In Sec. II we compare free space and cavity geometries in terms of

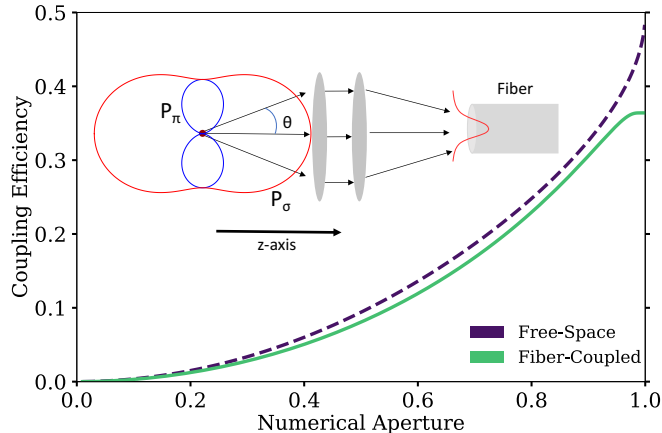


FIG. 2. Photon collection efficiency of a lens as a function of NA. The free-space collection efficiency (dashed line), shows the fraction of σ_{\pm} photons collected by the lens. The fiber-coupling efficiency from Eq. (1) (solid line), is the fraction of σ_{\pm} photons that are coupled into a single-mode fiber. The fiber-coupled efficiency is lower due to the finite mode-overlap of the σ_{\pm} photons and the fiber-mode at high NA. Emitted π polarized photons do not couple into the fiber.

their photon collection efficiency. In Sec. III we quantify the success probability for remote entanglement of two ^{87}Rb atoms in a cavity geometry. In Sec. IIIB we analyze achievable repetition rates, and the rate of entanglement generation, accounting for the need to periodically load and recool atoms. We conclude in Sec. IV with an outlook for implementation.

II. PHOTON COLLECTION EFFICIENCY - CAVITY VS. LENS

Efficient atom-photon coupling can be achieved with lenses or mirrors that have high NA or in resonant optical cavities. Lenses with NA up to 0.92 have been used in cold atom experiments, albeit at very short working distance⁴⁵. This implies that the atoms are trapped very close to a surface which is problematic when using Rydberg states that have high sensitivity to electric fields. Moreover, in experiments where the polarization of the photons matters large NA optics are not always beneficial as they can lead to polarization mixing. For example, in the entanglement scheme in a polarization basis, described below, collecting the unwanted polarization reduces the entanglement fidelity. Therefore, it is essential to couple the photons into single-mode fibers to reject the unwanted polarization. This also facilitates long-distance propagation as well as mode matching for Bell state measurements. However the fiber coupling efficiency decreases as the NA of the collection lens increases.

In this section, we calculate the collection efficiency for circularly polarized photons with a high NA lens, as

well as an optical cavity. Circularly polarized photons are considered in particular because of the entanglement scheme based on ^{87}Rb atoms that we consider in Sec. III. The atoms also emit π -polarized photons. However, the collection efficiency of the π -polarized photons is essentially zero. When collecting the photons along the quantization axis, as shown in the inset of Fig. 2, due to the destructive interference of the opposite parts of the field around the symmetric axis, the π -polarized photons do not couple into the single-mode fiber. Moreover, when the lens is replaced by an optical cavity, the π -polarized photons do not couple to the cavity mode lying along the quantization axis. Therefore, in this section, we assume a two-level emitter with a σ_{+} or σ_{-} transition only.

In Fig. 2 we plot the the coupling efficiency per atomic excitation η , which is the fraction of atomic excitation cycles that lead to a photon collected by the lens and coupled into the optical fiber. This is given by

$$\eta = \eta_{\text{col}} O \quad (1)$$

where η_{col} is the fraction of light collected by the lens and O is an overlap factor that determines the fraction of the collected light that is coupled into a propagating fiber mode. The fiber coupling efficiency is calculated by integrating the overlap between the dipole electric field \mathbf{E}_{D} of the atom and the Gaussian mode \mathbf{E}_{G} of the fiber

$$O = \left| \int_{\Omega} d\Omega \mathbf{E}_{\text{G}} \cdot \mathbf{E}_{\text{D}}^* \right|^2, \quad (2)$$

where Ω is the solid angle of the collection lens. We assume that the quantization axis is along the optical axis of the lens. The details of the calculation are provided in Appendix A. As shown in Fig. 2, as the NA approaches unity, 50% of the circularly polarized photons are collected by the lens; but less than 37% of the photons can be coupled into the fiber due to a poor overlap with the fiber mode. Calculations for a parabolic mirror show a very similar behavior.

Alternatively, a resonant optical cavity can be used to enhance the atom-photon coupling by orders of magnitude, and achieve an overall collection efficiency above 90% in a short cavity. In atom-cavity coupling, the key parameter that captures the ratio of coherent to dissipative interactions is the cooperativity C defined by⁴⁶

$$C = \frac{2g^2}{\kappa\gamma}, \quad (3)$$

where κ and γ are the full-width at half-maximum (FWHM) of the cavity and atomic decay rates, respectively⁴⁷. The vacuum Rabi frequency is

$$g = d\mathcal{E}/\hbar, \quad (4)$$

where d is the atomic transition matrix element, and \mathcal{E} is the vacuum electric field amplitude in a mode of frequency ω in the cavity, given by

$$\mathcal{E} = \left(\frac{\hbar\omega}{2\epsilon_0 V} \right)^{1/2}. \quad (5)$$

TABLE I. Demonstrations of remote entanglement of matter qubits. Additional remote entanglement protocols demonstrated between ensemble quantum memories^{31,32} and with superconducting qubits and microwave fields³³ are not included in the table.

Year	Research group	Description	qubit	rate (s ⁻¹)	fidelity
2007	Monroe ³⁴	remote ion-ion entanglement	¹⁷¹ Yb ⁺	0.0020	0.63
2008	Monroe ³⁵	remote ion-ion entanglement	¹⁷¹ Yb ⁺	0.026	0.81
2012	Rempel ¹⁴	remote quantum state transfer and entanglement	⁸⁷ Rb	100	0.85
2012	Weinfurter ³⁶	atom-atom entanglement	⁸⁷ Rb	0.0094	0.81
2013	Blatt ³⁷	ion-ion entanglement by photon detection	¹³⁸ Ba ⁺	0.23	0.64
2013	Hanson ³⁸	remote spin-spin entanglement	NV center	0.0017	0.68
2015	Monroe ³⁹	remote two ion-ion "modular" entanglement	¹⁷¹ Yb ⁺	4.5	0.78
2016	Imamoğlu ⁴⁰	remote entanglement hole spins	hole q. dots	2300.	0.55
2017	Weinfurter ⁴¹	atom-atom entanglement, loophole free Bell test	⁸⁷ Rb	~ 0.03	~ 0.85
2017	Atatüre ⁴²	remote spin-spin entanglement	InGaAs q. dot	7300.	0.62
2020	Lucas ⁴³	ion-ion entanglement	⁸⁸ Sr ⁺	182	0.94
2021	Hanson ⁴⁴	three-node network	NV center	9	0.81

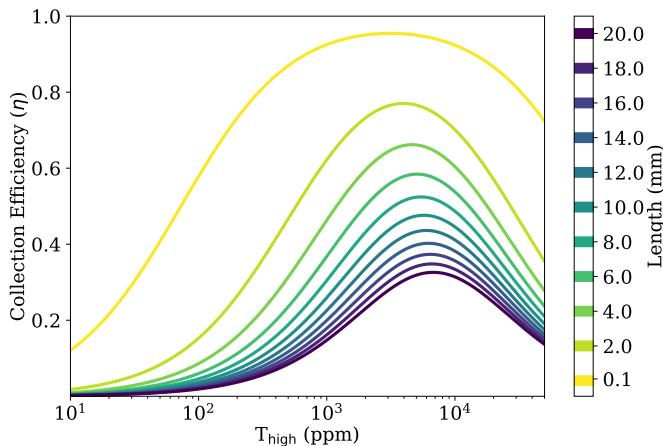


FIG. 3. Achievable collection efficiency η in an asymmetric near-concentric cavity as a function of mirror transmission for different cavity lengths. Parameters: $T_{\text{low}} = 10$ ppm, $\mathcal{L}_{RT} = 40$ ppm, $d_{\text{crit}} = 10 \mu\text{m}$, and $\gamma/2\pi = 6.07 \times 10^6 \text{ s}^{-1}$ corresponding to the ⁸⁷Rb D2 line.

Here, $V = \pi w_0^2 L/4$ is the effective mode volume for a TEM₀₀ resonator mode of length L and waist w_0 .

The overall collection efficiency of the cavity is defined as the fraction of atomic excitation cycles that lead to a photon coupled into the cavity mode and transmitted through the high transmission mirror. The collection efficiency is given by

$$\eta = \frac{2C}{1 + 2C} \frac{\kappa}{\kappa + \gamma} \frac{T_{\text{high}}}{T_{\text{low}} + T_{\text{high}} + \mathcal{L}_{RT}}. \quad (6)$$

The first factor indicates the fraction of photons coupled into the cavity mode. The second factor shows the probability that the photon leaves the cavity through one of the mirrors before being scattered again by the atom. The last fraction indicates the probability that the pho-

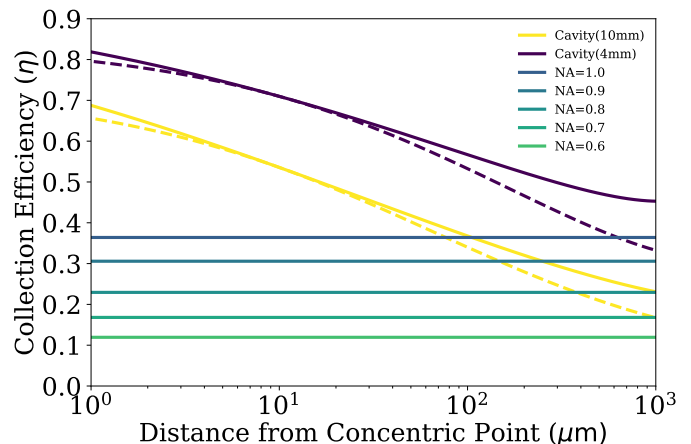


FIG. 4. Photon collection efficiency comparison between resonant cavities with different lengths and high-NA lenses. The collection efficiency of the cavities is calculated as a function of the distance from the concentric point d_{crit} . The purple and yellow lines representing η for the cavities are calculated using $T_{\text{low}} = 10$ ppm, $\mathcal{L}_{RT} = 40$ ppm. The solid lines are calculated with T_{high} having a value which maximizes η at each cavity length. The dashed lines show the value of η with T_{high} optimized for a cavity with $d_{\text{crit}} = 10 \mu\text{m}$. We have assumed that the fiber coupling from the TEM₀₀ cavity mode is unity.

ton leaves the cavity through the desired mirror with high transmission of T_{high} . Ideally, one wants the transmission of the other mirror, T_{low} , and the round-trip loss of the cavity due to mirror absorption and scattering, \mathcal{L}_{RT} , to be as small as possible. Note that in the limit of no excess cavity losses $T_{\text{low}} = \mathcal{L}_{RT} = 0$, the last term in Eq. (6) is unity and we recover the expression for the quantum efficiency given in⁴⁸. For all cavity geometries that we consider the mode width is several times larger than the optical wavelength, and in this limit the overlap factor of Eq. (2) is essentially unity, and therefore not included.

Equation (6) shows that efficient photon collection requires a relatively large cavity decay rate such that $\kappa/\gamma \gg 1$. However, the cavity decay should occur through only one of the mirrors. Thus, a highly asymmetric cavity is desired. We also note that the cooperativity depends on the mirror parameters as well. As we will show below, by adjusting the cavity parameters, such as the length and the mirror transmissions, the cavity can be tuned to the desired level of performance. It should be emphasized that while efficient photon collection does not depend on a particularly large C , other quantum operations between single atoms and photons such as state transfer or logic gates typically do require large cooperativity⁴⁹.

The cavity energy decay rate is

$$\kappa = \frac{\pi c}{L\mathcal{F}}, \quad (7)$$

where c is the speed of light in vacuum, and the finesse of an optical cavity with imperfect mirrors is given by

$$\mathcal{F} = \frac{\pi [(1 - T_{\text{low}})(1 - T_{\text{high}})(1 - \mathcal{L}_{\text{RT}})]^{1/4}}{1 - [(1 - T_{\text{low}})(1 - T_{\text{high}})(1 - \mathcal{L}_{\text{RT}})]^{1/2}}. \quad (8)$$

To achieve strong atom-light coupling a small waist is required since the cooperativity scales as \mathcal{F}/w_0^2 . It is often desirable to have a longer resonator without increasing the waist. This can be achieved in a near-concentric geometry for which

$$w_0 = w_{\text{nc}} = w_c \left(\frac{R_m - L/2}{L/2} \right)^{1/4}, \quad (9)$$

where $w_c = \sqrt{\frac{L\lambda}{2\pi}}$ is the waist for a confocal cavity, and R_m is the mirrors radius of curvature. When $R_m > L/2$ a stable mode with a waist much smaller than the confocal waist in a resonator of the same length is possible. Therefore, a near-concentric cavity offers excellent optical access for cooling and trapping atoms directly in the cavity mode while providing a small mode area necessary for strong coupling with the atoms.

However, to achieve a small mode area, the cavity has to operate near the stability limit. The stability parameter is defined by

$$s = 1 - \frac{L}{R_m}, \quad (10)$$

where $0 \leq s^2 \leq 1$ is required for a stable cavity. The cavity stability can be equivalently represented by the critical distance $d_{\text{crit}} = 2R_m - L$, i.e. the distance of the mirrors from the concentric point. Although a positive critical distance represents a stable cavity, maintaining alignment of a cavity with very small critical distance is challenging⁵⁰.

In Fig. 3 we show the photon collection efficiency of near-concentric cavities of various lengths calculated from Eq. (6). We see that a collection efficiency well

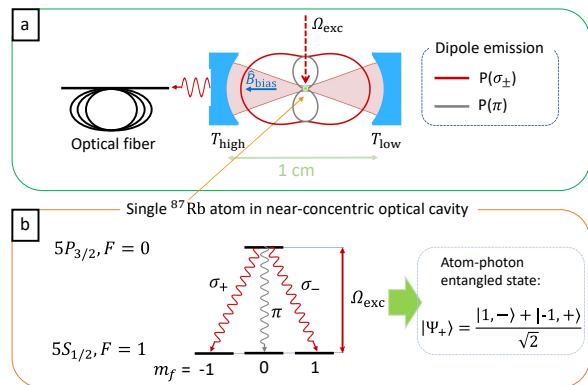


FIG. 5. a) Geometry for atom excitation and photon retrieval using a near-concentric optical cavity with higher mirror transmission on the fiber side. b) Relevant ^{87}Rb energy levels, decay and excitation scheme, and resulting atom-photon entangled state.

above 0.5 is achievable with a few-mm cavity length, and that the outcoupling mirror should have a certain transmission. With precise active alignment of the cavity mirrors near-concentric cavities with a critical distance less than a micron have been demonstrated⁵⁰. However, we assumed a moderate critical distance of $d_{\text{crit}} = 10 \mu\text{m}$.

In Fig. 4 we show the collection efficiency of near-concentric cavities with two different lengths as a function of the critical distance. The mirror radii of curvature for the long and short cavities are $R_m = 5 \text{ mm}$, and $R_m = 2 \text{ mm}$, respectively. As the critical distance changes, the required T_{high} to maximize the collection efficiency also changes. Thus, in the solid lines in Fig. 4 we optimize T_{high} at each critical distance. The dashed lines in Fig. 4 show the efficiency of the cavities with a T_{high} optimized for $d_{\text{crit}} = 10 \mu\text{m}$. For comparison, the figure also includes the collection efficiency of a lens at various numerical apertures. While the collection efficiency of a high NA lens is generally less than 30%, it is possible to collect more than 50% of the scattered photons by means of an optical cavity. In addition, when multiple decay channels are accessible to the excited atom an optical cavity can enhance the decay through the desired transitions, as we discuss below.

III. REMOTE ENTANGLEMENT PROTOCOL WITH ^{87}Rb ATOMS

Many different approaches to preparing remote entanglement have been proposed and demonstrated⁵¹. Table I lists a few earlier demonstrations of remote entanglement between matter qubits mediated by a photonic channel. Achieving high rates and high fidelity remains an out-

standing challenge in the field. In this section we provide a detailed analysis of the achievable rates using the atom-photon entanglement protocol shown in Fig. 5. A ^{87}Rb atom is trapped inside an optical resonator and prepared in the level $5s_{1/2}, f = 1$ by optical pumping. An excitation pulse of Rabi frequency Ω_{exc} transfers the atom to $5p_{3/2} |f = 0, m_f = 0\rangle$ from which the atom decays back to the $5s_{1/2}, f = 1$ level. Decay into $|f = 1, m_f = 0\rangle$ results in emission of a π -polarized photon that does not couple to the fiber through the optical cavity. Decay into $m_f = \pm 1$ is accompanied by emission of a σ_{\mp} photon which can couple to the cavity. Thus the observed coherent superposition is the entangled state

$$|\Psi_+\rangle = \frac{|1, \sigma_-\rangle + |-1, \sigma_+\rangle}{\sqrt{2}}. \quad (11)$$

In each ket, the first element shows the state of the atom, and the second element shows the state of the photon. The relative phase of the kets follows from the Clebsch-Gordan coefficients for the transitions.

Atom-photon entanglement with this choice of atomic states was demonstrated in Ref¹³ in a free-space geometry, and later extended to atom-atom entanglement³⁶ and a loophole-free Bell test⁴¹. In free-space, the emission rates are the same into all three magnetic sublevels. By using a resonant cavity the atomic decay rate into $m_f = \pm 1$ gets enhanced, while the decay into $m_f = 0$ is not affected by the cavity. Therefore, the effect of the cavity is two-fold: increasing the collection efficiency, as explained in Sec. II, and changing the branching ratio when multiple decay channels are available. For a transition coupled to the cavity mode, the overall decay rate is enhanced by a factor of $1 + 2C$ due to the Purcell effect⁵². Since two of the three possible transitions couple into the cavity, σ_{\pm} and π transitions occur with probabilities given by

$$P_+ = P_- = \frac{1 + 2C}{3 + 4C} \equiv P_{\sigma}, \quad (12)$$

$$P_{\pi} = \frac{1}{3 + 4C}. \quad (13)$$

We note that the total probability is normalized $P_+ + P_- + P_{\pi} = 1$. In the limit that the cooperativity C is zero, each transition occurs with 1/3 probability, as expected for transitions in free-space. Including P_{σ} Eq. (6) is modified to

$$\begin{aligned} \eta^{(\text{Rb})} &= 2P_{\sigma}\eta \\ &= \frac{4C}{3 + 4C} \frac{\kappa}{\kappa + \gamma} \frac{T_{\text{high}}}{T_{\text{low}} + T_{\text{high}} + \mathcal{L}_{\text{RT}}}. \end{aligned} \quad (14)$$

The dependence of $\eta^{(\text{Rb})}$ on the cavity parameters is shown in Fig. 6. Compared to the case of two-level atoms shown in Fig. 4, the resonant cavity collection efficiencies are reduced slightly, while all the free-space collection efficiencies are reduced by a factor of 2/3. Thus, the improvement provided by a cavity is more pronounced for

a real, multi-level atom. For a 10 mm resonant cavity with $d_{\text{crit}} = 10 \mu\text{m}$, $2P_{\sigma} \approx 90\%$. This clearly shows that both the increased collection efficiency, and the modification of the branching ratios contribute to the better performance of resonant cavities over free-space optics.

Examples of achievable quantum efficiency are given for a short confocal and two longer near-concentric cavity designs optimized for ^{87}Rb in Table II. Short cavities with small waists provide a high quantum efficiency. However, due to the limited optical access, laser cooling inside the cavity directly from a thermal background is impractical. Therefore, atom-transport from a cold atom source is required⁵³⁻⁵⁵ which lowers the overall rate of photon generation. To allow for cooling inside the cavity we consider a longer 10 mm near-concentric geometry without sacrificing the cavity mode area significantly. A medium-length 4 mm cavity gives a significant improvement to collection efficiency over the 10 mm cavity while still allowing for a magneto-optical trap (MOT) inside of the cavity. However, the required mirrors with small radius of curvature are not readily available.

As d_{crit} decreases in near-concentric cavities, the higher order spatial modes start to overlap with the fundamental mode of the cavity in frequency. Nevertheless, this is not a problem for the mm-scale cavities considered here. The frequency difference between the fundamental mode and the next transverse mode is¹⁰

$$\Delta\nu = \frac{c}{2L} \left(1 - \frac{\cos^{-1} s}{\pi} \right). \quad (15)$$

For the 10 mm and 4 mm cavities considered in Table II, the frequency spacing of the modes at $d_{\text{crit}} = 1 \mu\text{m}$ is 95 MHz and 377 MHz, respectively, which are several times larger than the cavity linewidths. Therefore, even at d_{crit} as small as $1 \mu\text{m}$, the transverse modes of the cavity are still non-degenerate.

A. Atom-Atom Entanglement Probability

To generate atom-atom remote entanglement atom-photon entanglement is generated at each node, and a Bell state measurement is made at the intermediate location as shown in Fig. 1. The probability of successful preparation of remote atom-atom entanglement on each attempt is

$$P_{\text{aa}} = \frac{1}{2} \left(\eta^{(\text{Rb})} \eta_{\text{det}} \right)^2, \quad (16)$$

where η_{det} is the quantum efficiency of the Bell state detectors, including any losses in fiber transmission. The factor of 1/2 accounts for the success probability of the Bell state measurement.

We can make an initial estimate of P_{aa} using $\eta^{(\text{Rb})} = 0.48$, the quantum efficiency of the 10 mm near-concentric cavity. The quantum efficiency of single photon counting modules (SPCMs) at 780 nm is ~ 0.7 , and the attenuation losses in the fiber can be described by $e^{-L_f/L_{\text{att}}}$ where L_f

TABLE II. Summary of cavity parameters optimized for ^{87}Rb . Examples given are those discussed in the text: a short confocal (e.g. optical fiber-based) cavity, and two lengths of longer near-concentric cavities. While the short cavity has the highest collection efficiency η , its length is prohibitive for cooling and trapping directly in the cavity as well as using Rydberg interactions between cavity and array qubits. The longer near-concentric cavities overcome these issues, while permitting a higher η than can be achieved with free-space optics. Other parameters are $T_{\text{low}} = 10$ ppm and $\mathcal{L}_{\text{RT}} = 40$ ppm.

	Short confocal	Medium near-concentric	Long near-concentric
L, R_m, w_0	(150, 150, 4.3) μm	3.99 mm, 2 mm, 4.98 μm	9.99 mm, 5 mm, 6.3 μm
$T_{\text{high}}, \mathcal{F}, C$	1540 ppm, 3950, 12.7	4620 ppm, 1346, 3.22	5730 ppm, 1080, 1.67
$(g, \kappa, \gamma)/2\pi$	(98, 253, 6) MHz	(17, 28, 6) MHz	(8.3, 14, 6) MHz
$\eta^{(\text{Rb})}$	0.89	0.66	0.48
P_{aa}	0.19	0.1	0.055

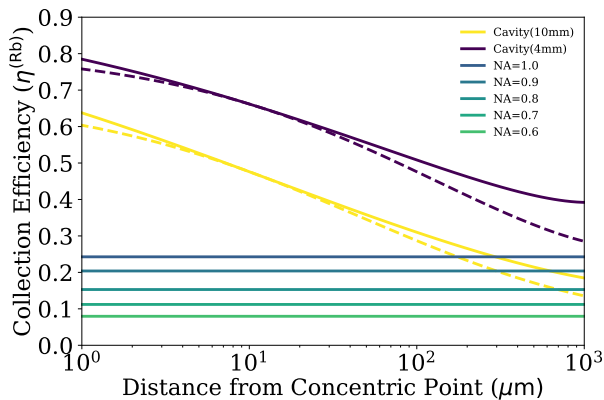


FIG. 6. Photon collection efficiency comparison between resonant cavities with different lengths and high-NA lenses for the ^{87}Rb entanglement scheme. Parameters are identical to Fig. 4 but now the branching ratios of the decaying atom are taken into account. The additional factor of $2P_\sigma$ makes the difference between free-space and cavity geometries more pronounced as closer to the concentric point a higher fraction of photons emitted by the atom go into the cavity mode. For the free-space collection the branching ratio is $2/3$.

is the fiber length in km and $L_{\text{att}} = 1.091$ km for a typical fiber at 780 nm. We will assume a fiber length of 10 m, such that the fiber losses are negligible. Therefore, with $\eta_{\text{det}} = 0.7$, we estimate that atom-atom entanglement can be generated with a probability of $P_{\text{aa}} = 5.6 \times 10^{-2}$.

B. Remote entanglement rate

The sequence of operations for preparing a two-atom entangled state is presented in Table III. Initially an atom is loaded into each dipole trap from a MOT. This is the most time consuming step which takes approximately $t_{\text{load}} = 100$ ms. Once atoms have been loaded into the traps they are pumped into the $5s_{1/2} |1, 0\rangle$ ground state, which takes approximately $t_{\text{pump}} = 6 \mu\text{s}$. The two atoms are then excited simultaneously with 30 ns π -pulses to the $5p_{3/2} |0, 0\rangle$ state. The SPCMs are gated for approximately 100 ns, a few times the excitation lifetime.

Proper detection of the spontaneously emitted photons from both nodes is critical for atom-atom entanglement to occur. Once the photons have been detected by the SPCMs we must determine if an appropriate photon-coincidence has occurred such that the two nodes have become entangled. This will occur with probability P_{aa} in each attempt following an estimated electronic processing time of $t_{\text{det}} \sim 1 \mu\text{s}$. Steps 2, 3 and 4 are repeated until a proper coincidence is registered between the SPCMs. The first four steps determine the achievable rate and how fast an entangled atom-atom pair can be generated.

To verify entanglement between the atoms we perform atom-state tomography in steps 5 through 8. First, we coherently transfer the population of $|1, 1\rangle$ to $|2, 1\rangle$ of the $5s_{1/2}$ ground state by a microwave π -pulse. Then, with two-photon microwave-radio frequency $\pi/2$ pulses^{56,57} we couple the states $|1, -1\rangle$ and $|2, 1\rangle$ to rotate the qubit states required for tomography. After qubit rotation, the population of $|2, 1\rangle$ is measured non-destructively²⁵.

Since the overall probability of establishing entanglement follows a binomial distribution, if we make N attempts at entanglement generation, the expected number of successful events is NP_{aa} , where P_{aa} is the atom-atom entanglement probability. Using the values in Table III and our estimated value of P_{aa} , we expect a single successful event on average every $N = 1/P_{\text{aa}} \approx 18$ attempts. The time to generate an entangled atom-atom pair once a trapped atom has been prepared is

$$t_{\text{aa}} \simeq N_{\text{epoch}}[N_1(t_{\text{pump}} + t_\pi + t_{\text{det}}) + t_{\text{cool}}], \quad (17)$$

where N_1 is the number of times that we address each atom between cooling cycles and N_{epoch} is the number of cooling cycles expected to be needed to generate atom-atom entanglement (see Fig. 7). The total number of attempts is $N = N_{\text{epoch}}N_1$. We want to choose a value for N_1 such that the probability of loss between cooling cycles is low enough that the expected lifetime of the trapped atom is background collision limited. Assuming a background limited lifetime for the atom in the trap of ~ 10 s with a trap depth of ~ 1 mK, and that each pumping cycle on average will scatter less than 5 photons, a reasonable value for N_1 is ~ 10 giving a probability of loss during the period of $N_1(t_{\text{pump}} + t_\pi + t_{\text{det}})$ of $< 0.01\%$. Assuming a cooling time of 100 μs , this gives an expected

TABLE III. Sequence of operations for a) preparing and b) verifying atom-atom entanglement.

Operation	Label	Duration	Success probability
a) Entanglement generation:			
1- prepare MOT, load into dipole trap	t_{load}	100 ms	> 0.99
2- pump to $5s_{1/2} 1, 0\rangle$	t_{pump}	6 μs	> 0.99
3- π -pulse to $5p_{3/2} 0, 0\rangle$	t_{π}	30 ns	> 0.99
4a- atomic decay, record and process photon clicks	t_{det}	1 μs	1
4b- cool atom if proper coincidence is not registered after $N_1 = 10$ cycles	t_{cool}	100 μs	> 0.99
b) Entanglement verification:			
5- map atomic qubit states $ 1, 1\rangle \rightarrow 2, 1\rangle$ with μ -wave π -pulse	$t_{\mu\text{w}}$	50 μs	~ 0.99
6- atomic qubit rotation with μ -wave + RF $\pi/2$ pulse	t_{rot}	500 μs	~ 0.98
7- non-destructive atomic state measurement	t_{m}	3 ms	$\sim 0.94^{25}$
8- cool atom to maintain localization in trap	t_{cool}	100 μs	> 0.99

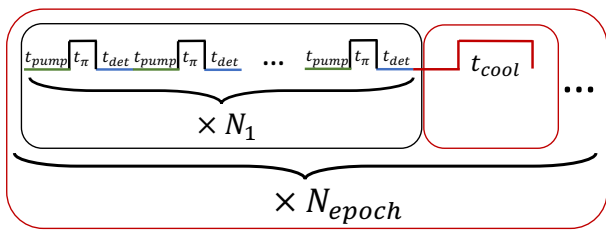


FIG. 7. Addressing sequence from Eq. (17). Referring to Table III, steps 2 and 3 are repeated N_1 times until either an entangled atom-atom pair is generated, or the atoms are cooled to continue addressing. The number of times that steps 2-4 need to be repeated on average to generate an entangled atom-atom pair is N_{epoch} .

lifetime of $>2\text{s}$ while continuously addressing and cooling the atom. This gives an average value for N_{epoch} of ~ 1.8 , and an expected time to generate atom-atom entanglement of

$$t_{\text{aa}} \simeq 1.8 \times [10(t_{\text{pump}} + t_{\pi} + t_{\text{det}}) + t_{\text{cool}}] \sim 0.31 \text{ ms}, \quad (18)$$

which results in an entanglement generation rate of $\sim 3200 \text{ s}^{-1}$.

These estimates are based on some assumptions. The most critical are that we can address the atom without loss due to a background collision, heating out of the trap, or depumping to $5s_{1/2}, f = 2$. Each time the atom is lost we would need to reload the trap resulting in $\sim 100 \text{ ms}$ of lost time, and a reduction in rate of $\sim 5\%$. We have assumed a Doppler cooling time of $100 \mu\text{s}$, which has been demonstrated in similar experiments⁴¹. The rates for these loss processes will have to be characterized and correction operations either inserted at a regular interval or performed after a fixed number of failed attempts. Leakage to $5s_{1/2}, f = 2$ can be rapidly corrected by shelving to $f = 1$ in less than $1 \mu\text{s}$ using light resonant with $5s_{1/2}, f = 2 \rightarrow 5p_{3/2}, f = 1$.

Figure 8 shows the possible rates achievable using the addressing sequence given in Eq. (17). t_{cool} sets a limit

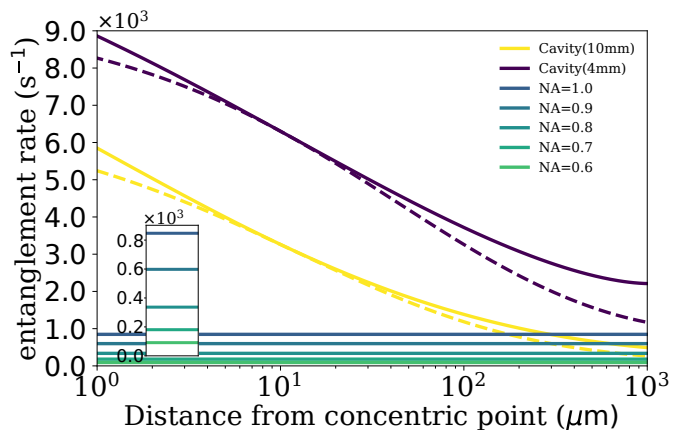


FIG. 8. Atom-atom entanglement generation rate for two cavity sizes and different high-NA lenses. The inset enlarges the rate of lenses for readability. Details are the same as Fig. 4.

on the rate assuming that cooling must happen after each entanglement generation event. The other factor which most significantly impacts the rate is the photon collection efficiency. Improving the collection efficiency will require either positioning the cavity closer to the concentric point, or using a smaller cavity. While a smaller cavity would provide a significant increase in the quantum efficiency, having a very small cavity that necessitates transporting the atoms into the cavity mode may be counter productive as the time required to do so is long and there is a large increase in complexity. Our goal is to have a cavity that is large enough that a MOT can be formed inside the cavity, and no atom-transport is required. Moving the cavity closer to the concentric point is a viable option as it has been demonstrated that a cavity in a near-concentric configuration can be maintained with $d_{\text{crit}} < 1 \mu\text{m}$ using active feedback⁵⁰. A similar spacing for a 10 mm cavity would decrease the mode volume by a factor of ~ 7 , and increase the value for P_{aa} by a

TABLE IV. Expected sources of atom-atom entanglement infidelity with their corresponding estimates.

Source of infidelity	Estimate(%)
Temporal overlap of photons ⁴³	5
Spatial overlap of photons ⁴³	1
Imperfect beamsplitter and waveplates ⁴³	0.2
Atom qubit rotation (for 2 atoms)	2
Atom state readout ²⁵ (for 2 atoms)	6
Atom qubit dephasing	negligible
Detector dark count	negligible
Multi-photon scattering	negligible
Off-resonant excitation	negligible
Total	14.2

factor of ~ 2 to 1.1×10^{-1} , and the rate to $\sim 5800 \text{ s}^{-1}$.

C. Atom-atom entanglement fidelity

The fidelity of the entangled state is defined as $F = \langle \Psi | \rho | \Psi \rangle$, where $|\Psi\rangle$ is the maximally entangled state heralded by the photons' Bell state measurement. The density matrix ρ of the entangled atom-atom state can be reconstructed through atom-state tomography. We anticipate that several factors can contribute to the loss of fidelity during the generation and verification of atom-atom entanglement. Table IV lists a few possible sources of infidelity with their estimated contribution. Assuming a dark count of less than 50 s^{-1} we estimate that the detectors dark counts have negligible effects on the fidelity. Since the photons are coupled into single-mode fibers, a good spatial overlap at the beamsplitter is expected.

An important source of infidelity is the non-perfect temporal overlap of the photons at the beamsplitter of the Bell state analyzer. This error is $[1 - \langle \alpha_1(t) | \alpha_2(t) \rangle] / 2$, where $\langle \alpha_1(t) | \alpha_2(t) \rangle$ is the temporal overlap integral of the two photons with amplitudes $\alpha_1(t)$ and $\alpha_2(t)$. We excite the two atoms at the two nodes simultaneously with a jitter time much smaller than the decay time of the excited state. Therefore, the two photons arrive at the beamsplitter at the same time with negligible error. However, the duration of the photon wave packets depend on the exact location of the atoms with respect to the anti-node of the cavities. If an atom is displaced from the cavity anti-node, the cooperativity decreases and consequently the lifetime of the atom in the cavity increases. By using optical tweezers to hold and place the atoms in the cavities, one can control the location of the atoms with a precision that scales as $w \sqrt{k_B T_a / U}$ where w is the waist of the optical tweezer, T_a is the atomic temperature, and U is the depth of the tweezer potential. With realistic parameters the localization can be better than 50 nm. Considering a more conservative error of 100 nm for the location of the atoms, we estimate an infidelity of 5% to due the non-perfect overlap of the photons.

Another important source of error is in non-destructive atom-state tomography. Based on previous experiments^{25,56}, we estimate that the atomic qubit can be rotated and measured with approximately 0.99 and 0.97 fidelity, respectively, at each node. Assuming a qubit coherence time of $T_2^* \sim 3 \text{ ms}$, which is dominated by magnetic noise and center of mass motion, and a delay of $t = 60 \mu\text{s}$ between photon detection and qubit measurements⁴³, we expect a loss of fidelity of order $e^{-(t/T_2^*)^2} \sim 4 \times 10^{-4}$ which is negligible. Since the relative phase of the atomic $|1, \pm 1\rangle$ Zeeman states is linearly sensitive to magnetic noise the local magnetic field must be well stabilized to prevent dephasing. Stabilization to better than 5 nT has been demonstrated using a feed forward approach⁵⁸ which is adequate for short photon transmission lengths.

The excitation scheme with π -polarized light prevents multi photon scattering into the cavity mode: when the atom emits a σ polarized photon, it decays to a superposition state that is not resonantly coupled by the π -polarized light to any excited state. Off-resonant excitation to $5p_{3/2}$ states with $f \geq 1$ is possible. However, the emitted photons from the higher excited states are not resonant to the cavity. Therefore, multi-photon scattering and off-resonant excitations do not reduce the entanglement fidelity. We also note that due to the birefringence of the optical fiber, the polarization state of the photons rotates upon propagation through the fiber. Thus, we maximize the fidelity by applying a unitary operation to the polarization state of the photons in post processing. Also, with the assumption that the cavity subtends a small solid angle, a slight misalignment between the cavity mode and the quantization axis contributes negligibly to the entanglement infidelity. Therefore, we estimate that achieving a fidelity of approximately 0.86 is realistic with the proposed scheme. We also note that the atom state tomography, which is the dominant source of infidelity, affects only the fidelity of the verification step. Therefore, the intrinsic fidelity of atom-atom entanglement can be well above 0.9.

IV. OUTLOOK

We have analyzed a two-species architecture that uses one species for networking, a second species for computation, and intra-species Rydberg gates to connect the computational register with the network. A near-concentric design provides high cooperativity in a geometry compatible with in-situ atom cooling, which removes the need for atom transport, and thereby increases the repetition rate of the entanglement generating steps.

Assuming a short optical fiber link of 10 m remote entanglement rates of several hundred s^{-1} are possible using free space collection optics, and several thousand s^{-1} with resonant cavities. For longer links these rates will be reduced due to fiber attenuation. To avoid this it is necessary to convert to low loss telecom wavelengths. This

can be done with appropriate atomic transitions in Rb, or other atoms^{7,59}, or by conversion in nonlinear optical media⁶⁰.

In order to extend the reach of quantum networks to even longer distances multiple steps of remote entanglement are needed. The node architecture of Fig. 1 can serve as a building block for a quantum repeater based network. Incorporating the capability for writing photonic states onto communication atoms, and then performing local entangling gates, will enable deterministic Bell state measurements. In this way the factor of 1/2 in Eq. (16) can be removed, which will increase the entanglement distribution rate.

V. ACKNOWLEDGMENT

This material is based upon work supported by the U.S. Department of Energy Office of Science National Quantum Information Science Research Centers and support from NSF Award 2016136 for the QLCI center Hybrid Quantum Architectures and Networks. AS acknowledges the support of the Natural Sciences and Engineering Research Council of Canada (NSERC), [funding reference number PDF - 546105 - 2020]. CBY and AS contributed equally to the manuscript.

- ¹C. Monroe, R. Raussendorf, A. Ruthven, K. R. Brown, P. Maunz, L.-M. Duan, and J. Kim, “Large-scale modular quantum-computer architecture with atomic memory and photonic interconnects,” *Phys. Rev. A* **89**, 022317 (2014).
- ²M. Morgado and S. Whitlock, “Quantum simulation and computing with Rydberg-interacting qubits,” *AVS Qu. Sci.* **3**, 021101 (2021).
- ³T. M. Graham, Y. Song, J. Scott, C. Poole, L. Phuttitarn, K. Jooya, P. Eichler, X. Jiang, A. Marra, B. Grinkemeyer, M. Kwon, M. Ebert, J. Cherek, M. T. Lichtman, M. Gillette, J. Gilbert, D. Bowman, T. Ballance, C. Campbell, E. D. Dahl, O. Crawford, N. S. Blunt, B. Rogers, T. Noel, and M. Saffman, “Multi-qubit entanglement and algorithms on a neutral-atom quantum computer,” *Nature* **604**, 457–462 (2022).
- ⁴D. Bluvstein, H. Levine, G. Semeghini, T. T. Wang, S. Ebadi, M. Kalinowski, A. Keesling, N. Maskara, H. Pichler, M. Greiner, V. Vuletić, and M. D. Lukin, “A quantum processor based on coherent transport of entangled atom arrays,” *Nature* **604**, 451–456 (2022).
- ⁵M. Saffman, T. G. Walker, and K. Mølmer, “Quantum information with Rydberg atoms,” *Rev. Mod. Phys.* **82**, 2313–2363 (2010).
- ⁶A. Asenjo-Garcia, M. Moreno-Cardoner, A. Albrecht, H. J. Kimble, and D. E. Chang, “Exponential improvement in photon storage fidelities using subradiance and “selective radiance” in atomic arrays,” *Phys. Rev. X* **7**, 031024 (2017).
- ⁷J. P. Covey, A. Sipahigil, S. Szoke, N. Sinclair, M. Endres, and O. Painter, “Telecom-band quantum optics with ytterbium atoms and silicon nanophotonics,” *Phys. Rev. Appl.* **11**, 034044 (2019).
- ⁸S. G. Menon, K. Singh, J. Borregaard, and H. Bernien, “Nanophotonic quantum network node with neutral atoms and an integrated telecom interface,” *New J. Phys.* **22**, 073033 (2020).
- ⁹T. Đorđević, P. Samutpraphoot, P. L. Ocola, H. Bernien, B. Grinkemeyer, I. Dimitrova, V. Vuletić, and M. D. Lukin, “Entanglement transport and a nanophotonic interface for atoms in optical tweezers,” *Science* **373**, 1511 (2021).
- ¹⁰C. H. Nguyen, A. N. Utama, N. Lewty, K. Durak, G. Maslennikov, S. Straupe, M. Steiner, and C. Kurtsiefer, “Single atoms coupled to a near-concentric cavity,” *Phys. Rev. A* **96**, 031802(R) (2017).
- ¹¹A. Kawasaki, B. Braverman, E. Pedrozo-Peñafiel, C. Shu, S. Colombo, Z. Li, O. Özel, W. Chen, L. Salvi, A. Heinz, D. Levonian, D. Akamatsu, Y. Xiao, and V. Vuletić, “Geometrically asymmetric optical cavity for strong atom-photon coupling,” *Phys. Rev. A* **99**, 013437 (2019).
- ¹²W. Huie, S. G. Menon, H. Bernien, and J. P. Covey, “Multiplexed telecommunication-band quantum networking with atom arrays in optical cavities,” *Phys. Rev. Res.* **3**, 043154 (2021).
- ¹³J. Volz, M. Weber, D. Schlenk, W. Rosenfeld, J. Vrana, K. Saucke, C. Kurtsiefer, and H. Weinfurter, “Observation of entanglement of a single photon with a trapped atom,” *Phys. Rev. Lett.* **96**, 030404 (2006).
- ¹⁴S. Ritter, C. Nölleke, C. Hahn, A. Reiserer, A. Neuzner, M. Uphoff, M. Mücke, E. Figueroa, J. Bochmann, and G. Rempe, “An elementary quantum network of single atoms in optical cavities,” *Nature* **484**, 195–200 (2012).
- ¹⁵M. Uphoff, M. Brekenfeld, G. Rempe, and S. Ritter, “An integrated quantum repeater at telecom wavelength with single atoms in optical fiber cavities,” *Appl. Phys. B* **122**, 46 (2016).
- ¹⁶M. Saffman and T. G. Walker, “Creating single-atom and single-photon sources from entangled atomic ensembles,” *Phys. Rev. A* **66**, 065403 (2002).
- ¹⁷M. Saffman and T. G. Walker, “Entangling single- and N-atom qubits for fast quantum state detection and transmission,” *Phys. Rev. A* **72**, 042302 (2005).
- ¹⁸L. Li, Y. O. Dudin, and A. Kuzmich, “Entanglement between light and an optical atomic excitation,” *Nature* **498**, 466 (2013).
- ¹⁹D. Petrosyan and K. Mølmer, “Deterministic free-space source of single photons using Rydberg atoms,” *Phys. Rev. Lett.* **121**, 123605 (2018).
- ²⁰A. Grankin, P. O. Guimond, D. V. Vasilyev, B. Vermersch, and P. Zoller, “Free-space photonic quantum link and chiral quantum optics,” *Phys. Rev. A* **98**, 043825 (2018).
- ²¹Y. Zeng, P. Xu, X. He, Y. Liu, M. Liu, J. Wang, D. J. Papoular, G. V. Shlyapnikov, and M. Zhan, “Entangling two individual atoms of different isotopes via Rydberg blockade,” *Phys. Rev. Lett.* **119**, 160502 (2017).
- ²²I. I. Beterov and M. Saffman, “Rydberg blockade, Förster resonances, and quantum state measurements with different atomic species,” *Phys. Rev. A* **92**, 042710 (2015).
- ²³K. Singh, S. Anand, A. Pocklington, J. T. Kemp, and H. Bernien, “Dual-element, two-dimensional atom array with continuous-mode operation,” *Phys. Rev. X* **12**, 011040 (2022).
- ²⁴I. V. Inlek, C. Crocker, M. Lichtman, K. Sosnova, and C. Monroe, “Multispecies trapped-ion node for quantum networking,” *Phys. Rev. Lett.* **118**, 250502 (2017).
- ²⁵M. Kwon, M. F. Ebert, T. G. Walker, and M. Saffman, “Parallel low-loss measurement of multiple atomic qubits,” *Phys. Rev. Lett.* **119**, 180504 (2017).
- ²⁶J. P. Covey, A. Sipahigil, and M. Saffman, “Microwave-to-optical conversion via four-wave-mixing in a cold ytterbium ensemble,” *Phys. Rev. A* **100**, 012307 (2019).
- ²⁷A. E. B. Nielsen and K. Mølmer, “Deterministic multimode photonic device for quantum-information processing,” *Phys. Rev. A* **81**, 043822 (2010).
- ²⁸A. C. J. Wade, M. Mattioli, and K. Mølmer, “Single-atom single-photon coupling facilitated by atomic-ensemble dark-state mechanisms,” *Phys. Rev. A* **94**, 053830 (2016).
- ²⁹I. Cohen and K. Mølmer, “Deterministic quantum network for distributed entanglement and quantum computation,” *Phys. Rev. A* **98**, 030302 (2018).
- ³⁰J. Calsamiglia and N. Lütkenhaus, “Maximum efficiency of a linear-optical Bell-state analyzer,” *Appl. Phys. B* **72**, 67 (2001).
- ³¹K. S. Choi, A. Goban, S. B. Papp, S. J. van Enk, and H. J. Kimble, “Entanglement of spin waves among four quantum memories,” *Nature* **468**, 412 (2010).
- ³²Y. Yu, F. Ma, X.-Y. Luo, B. Jing, P.-F. Sun, R.-Z. Fang, C.-W. Yang, H. Liu, M.-Y. Zheng, X.-P. Xie, W.-J. Zhang, L.-X. You,

- Z. Wang, T.-Y. Chen, Q. Zhang, X.-H. Bao, and J.-W. Pan, “Entanglement of two quantum memories via fibres over dozens of kilometres,” *Nature* **578**, 240 (2020).
- ³³A. Narla, S. Shankar, M. Hatridge, Z. Leghtas, K. M. Sliwa, E. Zalys-Geller, S. O. Mundhada, W. Pfaff, L. Frunzio, R. J. Schoelkopf, and M. H. Devoret, “Robust concurrent remote entanglement between two superconducting qubits,” *Phys. Rev. X* **6**, 031036 (2016).
- ³⁴D. L. Moehring, P. Maunz, S. Olmschenk, K. C. Younge, D. N. Matsukevich, L.-M. Duan, and C. Monroe, “Entanglement of single-atom quantum bits at a distance,” *Nature* **449**, 68 (2007).
- ³⁵D. N. Matsukevich, P. Maunz, D. L. Moehring, S. Olmschenk, and C. Monroe, “Bell inequality violation with two remote atomic qubits,” *Phys. Rev. Lett.* **100**, 150404 (2008).
- ³⁶J. Hofmann, M. Krug, N. Ortegel, L. Gérard, M. Weber, W. Rosenfeld, and H. Weinfurter, “Heralded entanglement between widely separated atoms,” *Science* **337**, 72–75 (2012).
- ³⁷L. Slodička, G. Hétet, N. Röck, P. Schindler, M. Hennrich, and R. Blatt, “Atom-atom entanglement by single-photon detection,” *Phys. Rev. Lett.* **110**, 083603 (2013).
- ³⁸H. Bernien, B. Hensen, W. Pfaff, G. Koolstra, M. S. Blok, L. Robledo, T. H. Taminiau, M. Markham, D. J. Twitchen, L. Childress, and R. Hanson, “Heralded entanglement between solid-state qubits separated by three metres,” *Nature* **497**, 86 (2013).
- ³⁹D. Hucul, I. V. Inlek, G. Vittorini, C. Crocker, S. Debnath, S. M. Clark, and C. Monroe, “Modular entanglement of atomic qubits using photons and phonons,” *Nat. Phys.* **11**, 37 (2015).
- ⁴⁰A. Delteil, Z. Sun, W. b. Gao, E. Togan, S. Faelt, and A. Imamoglu, “Generation of heralded entanglement between distant hole spins,” *Nat. Phys.* **12**, 218 (2016).
- ⁴¹W. Rosenfeld, D. Burchardt, R. Garthoff, K. Redeker, N. Ortegel, M. Rau, and H. Weinfurter, “Event-ready Bell test using entangled atoms simultaneously closing detection and locality loopholes,” *Phys. Rev. Lett.* **119**, 010402 (2017).
- ⁴²R. Stockill, M. J. Stanley, L. Huthmacher, E. Clarice, M. Hugues, A. J. Miller, C. Matthiesen, C. Le Gall, and M. Atatüre, “Phase-tuned entangled state generation between distant spin qubits,” *Phys. Rev. Lett.* **119**, 010503 (2017).
- ⁴³L. J. Stephenson, D. P. Nadlinger, B. C. Nichol, S. An, P. Dromota, T. G. Ballance, K. Thirumalai, J. F. Goodwin, D. M. Lucas, and C. J. Ballance, “High-rate, high-fidelity entanglement of qubits across an elementary quantum network,” *Phys. Rev. Lett.* **124**, 110501 (2020).
- ⁴⁴M. Pompili, S. L. N. Hermans, S. Baier, H. K. C. Beukers, P. C. Humphreys, R. N. Schouten, R. F. L. Vermeulen, M. J. Tiggelman, L. dos Santos Martins, B. Dirkse, S. Wehner, and R. Hanson, “Realization of a multinode quantum network of remote solid-state qubits,” *Science* **372**, 259 (2021).
- ⁴⁵C. Robens, S. Brakhane, W. Alt, F. Kleiðler, D. Meschede, G. Moon, G. Ramola, and A. Alberti, “High numerical aperture (NA = 0.92) objective lens for imaging and addressing of cold atoms,” *Opt. Lett.* **42**, 1043 (2017).
- ⁴⁶A. Reiserer and G. Rempe, “Cavity-based quantum networks with single atoms and optical photons,” *Rev. Mod. Phys.* **87**, 1379 (2015).
- ⁴⁷The equation for C in⁴⁶ appears different than our definition because those authors use κ, γ defined as FWHM/2.
- ⁴⁸G. Cui and M. G. Raymer, “Quantum efficiency of single-photon sources in the cavity-QED strong-coupling regime,” *Opt. Expr.* **13**, 9660 (2005).
- ⁴⁹S. Daiss, S. Langenfeld, S. Welte, E. Distanto, P. Thomas, L. Hartung, O. Morin, and G. Rempe, “A quantum-logic gate between distant quantum-network modules,” *Science* **371**, 614 (2021).
- ⁵⁰C. H. Nguyen, A. N. Utama, N. Lewty, and C. Kurtsiefer, “Operating a near-concentric cavity at the last stable resonance,” *Phys. Rev. A* **98**, 063833 (2018).
- ⁵¹D. L. Moehring, M. J. Madsen, K. C. Younge, J. R. N. Kohn, P. Maunz, L.-M. Duan, C. Monroe, and B. B. Blinov, “Quantum networking with photons and trapped atoms,” *J. Opt. Soc. AM.* **B 24**, 300 (2007).
- ⁵²E. Purcell, “Spontaneous emission probabilities at radio frequencies,” *Phys. Rev.* **69**, 681 (1946).
- ⁵³K. M. Fortier, S. Y. Kim, M. J. Gibbons, P. Ahmadi, and M. S. Chapman, “Deterministic loading of individual atoms to a high-finesse optical cavity,” *Phys. Rev. Lett.* **98**, 233601 (2007).
- ⁵⁴J. Gallego, W. Alt, T. Macha, M. Martinez-Dorantes, D. Pandey, and D. Meschede, “Strong Purcell effect on a neutral atom trapped in an open fiber cavity,” *Phys. Rev. Lett.* **121**, 173603 (2018).
- ⁵⁵G. T. Hickman and M. Saffman, “Speed, retention loss, and motional heating of atoms in an optical conveyor belt,” *Phys. Rev. A* **101**, 063411 (2020).
- ⁵⁶D. M. Harber, H. J. Lewandowski, J. M. McGuirk, and E. A. Cornell, “Effect of cold collisions on spin coherence and resonance shifts in a magnetically trapped ultracold gas,” *Phys. Rev. A* **66**, 053616 (2002).
- ⁵⁷P. Treutlein, P. Hommelhoff, T. Steinmetz, T. W. Hänsch, and J. Reichel, “Coherence in microchip traps,” *Phys. Rev. Lett.* **92**, 203005 (2004).
- ⁵⁸B. Merkel, K. Thirumalai, J. E. Tarlton, V. M. Schäfer, C. J. Ballance, T. P. Harty, and D. M. Lucas, “Magnetic field stabilization system for atomic physics experiments,” *Rev. Sci. Instrum.* **90**, 044702 (2019).
- ⁵⁹A. G. Radnaev, Y. O. Dudin, R. Zhao, H. H. Jen, S. D. Jenkins, A. Kuzmich, and T. A. B. Kennedy, “A quantum memory with telecom-wavelength conversion,” *Nat. Phys.* **6**, 894–899 (2010).
- ⁶⁰A. Dréau, A. Tchebotareva, A. E. Mahdaoui, C. Bonato, and R. Hanson, “Quantum frequency conversion of single photons from a nitrogen-vacancy center in diamond to telecommunication wavelengths,” *Phys. Rev. Appl.* **9**, 064031 (2018).

VI. APPENDIX

A. Fiber coupling efficiency of a high-NA lens

To calculate the coupling efficiency of the scattered photons into a single-mode fiber, we assume that the fiber supports a Gaussian mode. In other words, we assume that a Gaussian mode can be coupled into the fiber with 100% efficiency. Thus, we find the field distribution of the radiating dipole after the collection lens, i.e. between the two lenses shown in Fig. 2, and calculate its overlap with a collimated Gaussian mode.

Referring to the geometry shown in the inset of Fig. 2, the three components of the electric field of a radiating dipole are given by

$$\mathbf{E}_{\sigma_{\pm}}(\theta, \phi) = \sqrt{\frac{3}{16\pi}} \frac{ie^{i(kr \pm \phi)}}{r} (\pm \cos \theta \hat{\theta} + i \hat{\phi}) \quad (19)$$

$$\mathbf{E}_{\pi}(\theta, \phi) = \sqrt{\frac{3}{16\pi}} \frac{ie^{i\phi}}{r} \sin \theta \hat{\theta}, \quad (20)$$

where ϕ is the azimuthal angle. After passing through the collection lens, the spherical coordinates are transformed in the following way

$$\begin{aligned} \hat{\theta} &\rightarrow \hat{\rho} \\ \hat{r} &\rightarrow \hat{z} \\ \hat{\phi} &\rightarrow \hat{\phi} \end{aligned}$$

Converting Eqs. (19) and (20) to cylindrical coordinates gives the following expressions for the field amplitudes

after the collection lens

$$\mathbf{E}_{\sigma\pm}(\rho, \phi) = \sqrt{\frac{3}{16\pi}} \frac{ie^{\pm i\phi} f^{1/2}}{(f^2 + \rho^2)^{3/4}} \left[\frac{\pm f}{(f^2 + \rho^2)^{1/2}} \hat{\rho} + i\hat{\phi} \right], \quad (21)$$

$$\mathbf{E}_{\pi}(\rho, \phi) = \sqrt{\frac{3}{16\pi}} \frac{ie^{\pm i\phi} f^{1/2}}{(f^2 + \rho^2)^{3/4}} \frac{\rho}{(f^2 + \rho^2)^{1/2}} \hat{\rho}, \quad (22)$$

where f is the focal length of the lens, ρ is the radial coordinate from the axis of the lens, and the factor of $f^{1/2}/(f^2 + \rho^2)^{1/4}$ ($\sqrt{\cos\theta}$ in spherical coordinates before the lens) accounts for the projection of the field onto the lens plane. Note that in both coordinate systems the integral of the dipole field $\mathbf{E}_D = \mathbf{E}_{\sigma\pm}$ or $\mathbf{E}_D = \mathbf{E}_{\pi}$ over half of the full solid angle gives half of the total energy emitted by the dipole

$$\int_0^{\pi/2} d\theta \sin\theta \int_0^{2\pi} d\phi |\mathbf{E}_D(\theta, \phi)|^2 = \frac{1}{2}, \quad (23)$$

$$\int_0^{\infty} d\rho \rho \int_0^{2\pi} d\phi |\mathbf{E}_D(\rho, \phi)|^2 = \frac{1}{2}. \quad (24)$$

The field of a circularly polarized Gaussian laser mode

with waist w is given by

$$\mathbf{E}_G = \frac{1}{\sqrt{\pi}w} e^{-\frac{\rho^2}{w^2}} \left[(\cos\phi \pm i \sin\phi) \hat{\rho} - (\sin\phi \mp i \cos\phi) \hat{\phi} \right]. \quad (25)$$

We then calculate the overlap integral of the collimated dipole field, Eqs. (21) and (22), with the Gaussian mode of Eq.(25):

$$O = \left| \int_0^{\rho_{\text{NA}}} d\rho \rho \int_0^{2\pi} d\phi \mathbf{E}_G \cdot \mathbf{E}_D^* \right|^2, \quad (26)$$

where $\rho_{\text{NA}} = \frac{f\text{NA}}{\sqrt{1-(\text{NA})^2}}$. From this integral we see that the overlap of the π -polarized light emitted by the atom and the Gaussian mode is zero. Thus, the π -polarized photons do not couple into the single-mode fiber. We also calculate the overlap of the circularly polarized light emitted by the atom with the Gaussian mode which is shown in Fig. 2. As the NA of the lens changes, the beam waist w in Eq. (25) has to be adjusted to maximize the overlap integral.

We note that the transverse profile of the photons collected and collimated by the lens is not Gaussian. Also, the polarization of the photons changes gradually from circular at the center ($\rho = 0$) to elliptical as ρ increases. Both of these effects contribute to decreasing the overlap integral in Eq. (26).